
Impact of realistic properties of the point spread function on classification tasks to reveal a possible distribution shift

Anonymous Author(s)

Affiliation

Address

email

Abstract

1 Image classification is a long-standing task in computer vision with deep neural
2 networks (DNN) producing excellent results on various challenges. However, they
3 are required not only to perform highly accurate on benchmarks such as ImageNet,
4 but also to robustly handle images in adverse conditions, such as modified light-
5 ing, sharpness, weather conditions and image compression. Various benchmarks
6 aimed to measure robustness show that neural networks perform differently well
7 under distribution shifts. While datasets such as ImageNet-C model for example
8 common corruptions such as blur and adverse weather conditions, we argue that
9 the properties of the optical system and the potentially resulting complex lens blur
10 are insufficiently well studied in the literature. This study evaluates the impact of
11 realistic optical corruptions on the ImageNet classification. The proposed complex
12 corruption kernels are direction and wavelength dependent and include chromatic
13 aberration, which are all to be expected in realistic scenarios such as autonomous
14 driving applications. Our experiments on twelve different DNN models show sig-
15 nificant differences of more than 5% in the top1 classification error, when compared
16 to the model performances on matched ImageNet-C blur kernels.

17 1 Introduction

18 Neural networks for computer vision tasks are used in a wide range of applications and are expected
19 to be reliable in safety-critical situations such as in autonomous driving [1, 2, 3]. Therefore, it is
20 crucial that neural networks are able to generalize from the training distribution to unknown images
21 and slight domain shifts. In order to test such behavior, various benchmarks have been proposed
22 that introduce targeted corruptions [4, 5, 6, 7] or mimic common corruptions and adverse weather
23 conditions [8, 9]. The simulation of effects such as lighting conditions, noise or image sharpness
24 have been addressed for examples by Hendrycks et al. [8]. In [9], Kar et al. aim for more realistic
25 modeling by proposing additional 3D corruptions such as change of field of view, camera roll or far
26 focus.

27 While these papers cover a wide range of corruptions, they introduce necessary simplifications for
28 each of them. As a result, they do not consider complex corruptions as they can result from the optical
29 recording system. In this paper, we argue that the modeling of such realistic optical blur kernels that
30 include chromatic aberrations and astigmatism should be considered, since they are very likely to
31 eventually occur in practice.

32 Thus, we examine the effects of two complex kernel types on ImageNet and evaluate on the resulting
33 corruptions the behavior of existing, robust and non-robust classification models, using ImageNet-C
34 [8] as a baseline.

35 Practically, the image of an object plane produced by a lens can be described using linear systems
 36 theory: If an idealized point light source is propagated through a camera’s objective lens, the point
 37 function is spread to some degree on the image side. This observed intensity function is therefore
 38 called the intensity point *spread* function (PSF). In the best case, the PSF is diffraction-limited and
 39 therefore small and rotationally-symmetric. As a rule, however, the optical system is not perfectly
 40 balanced and aberrations arise. These aberrations directly affect the observed PSF. Thus, non-
 41 rotationally symmetric shapes that differ in wavelength can often occur and show the effects of
 42 e.g. Astigmatism and chromatic aberration. PSF examples are given in the appendix A. In general,
 43 the PSF varies over the image field. The superposition of all these point responses weighted with the
 44 scene’s intensity yields the observed image.[10, 11] By means of simulation, such PSFs applied to an
 45 image can mimic the capture with the virtual lens model. For simplicity, we assume isoplanarity such
 46 that a single PSF represents a virtual lens, but with a focus on directional and wavelength dependence
 47 in contrast to approximate rotational symmetric blur kernels such as assumed in ImageNet-C[8].

48 **2 Analysis of the impact of realistic PSF properties to classification**

49 This article investigates the impact of directional and wavelength dependent PSFs at different
 50 severities. The optically motivated kernels will be called optical kernels here in contrast to the
 51 corruption kernels from ImageNet-C .

52 We take the defocus blur kernels from ImageNet-C and compare to them in size approximate matched
 53 optical kernels. Subsequently the image datasets (defocus blur from ImageNet-C and the proposed
 54 optical kernels) are classified by different pretrained neural networks. We compare the results for all
 55 severities of classification and image degradation. All operations are done in python and pytorch.
 56 Google Colab GPUs are used to perform the inference for the image datasets and to perform the
 57 different image dataset comparisons.

58 **2.1 Metrics**

59 To compare the data, different metrics are used following the dataflow from a set of PSFs to
 60 images (IMG) and classification (CLS). First, PSFs are generated, see Figure 1(left). From this,
 61 the modulation transfer function (MTF) can be generated, which is an established optical quality
 62 metric.[12, 13] The two-dimensional function is given in pairs of orthogonal slices in a particular
 63 direction, e.g. in direction of the coordinate axes or in diagonal direction. There exist different
 64 functionals derived from the MTF curve such as MTF50, which denotes the frequency value where
 65 the MTF falls to 50 %, and area under the curve (AUC), which is the integral of the MTF. The metrics
 66 are meaningful, if curves of similar shape are compared to ensure for example for AUC, that the
 67 intensity is concentrated in similar frequency regions. These curves are used to match the corruption
 68 kernels and optical kernels.

69 The application of each PSF kernel to ImageNet yields a modified image dataset for each severity,
 70 which is compared to the unmodified ImageNet validation dataset. Every image of a modified dataset
 71 is compared to the unmodified original. These comparisons are evaluated with mean squared error
 72 (MSE) and the structural similarity index (SSIM).[14] To obtain a manageable overview, the means
 73 of these metrics are taken and are denoted as mMSE and mSSIM respectively.

74 These images are then fed to the different classifiers. The classifiers are assessed with the top1-error,
 75 which takes the mean of all falsely classified images. These values are then compared for the different
 76 models and for each severity.

77 **2.2 Blur models**

78 The corruption kernels represent the reproduced "defocus blur" corruption kernels from ImageNet-C
 79 for five severities. The generation of these kernels is a two step process: First, a disk shape is created,
 80 which is then blurred with Gaussian blur.[8] This yields approximate rotationally symmetric blur
 81 kernels, which do not depend on the color channel and model defocus.

82 To compare such kernels with more realistic optical kernels, we use the color-dependent average PSF
 83 of a space-variant Cooke-Triplet lens model [15] as base PSF:

$$h(u, v, \lambda) = |\mathcal{F}\{(P(x, y) \cdot e^{-j2\pi W_\lambda(x, y, \lambda)})\}|^2, \quad (1)$$

84 where h denominates the intensity PSF acquired from a complex pupil description consisting of
 85 the pupil shape P and its phase with the real wavefront aberration W_λ . [11] For the average PSF a
 86 wavefront aberration description W_λ is available from [15] in terms of Zernike Polynomials Z_n^m [10]:

$$W_\lambda(x, y, \lambda) = \lambda \cdot \sum_{n,m} A_n^m(\lambda) \cdot Z_n^m \quad (2)$$

87 Each coefficient A_n^m in multiples of the wavelengths $\lambda_i \in \{0.4861 \mu\text{m}, 0.5876 \mu\text{m} \text{ and } 0.6563 \mu\text{m}\}$
 88 represents the contribution of a particular type of aberration. This allows to parameterize different
 89 aspects such as the amount of coma, astigmatism or defocus. The base PSF's wavefront aberration
 90 description therefore consists of three different sets of the first 20 Zernike-Fringe coefficients,
 91 which are then assigned to the different RGB color channels. To show directional dependence,
 92 oblique astigmatism A_2^{-2} is varied, which may also lead to chromatic aberration: The original
 93 wavefront aberration W depends on wavelength. The experimentally determined parameterization
 94 $A_2^{-2} \in \{1, 1.4, 2, 3, 3.8\} \lambda_i$ leads to optical kernels comparable to the corruption kernels both in
 95 terms of PSF metrics (MTF50, AUC, MTF curves) as well as IMG metrics (SSIM, MSE).

96 We also include two additional studies in appendix C for "straight" astigmatism and a closer matched
 97 version for oblique astigmatism.

98 3 Experiments on ImageNet

99 We select 12 pretrained neural networks for classification with common architectures [16] from Tab.
 100 1. All models are pretrained on ImageNet and publicly available from pytorch vision's model zoo. We
 101 also include three models with ResNet50 architecture from the RobustBench's model zoo [7] ranked
 102 under the top-5 networks at the ImageNet leaderboard for corruptions. [7] These neural networks are
 103 robust on ImageNet-C [8] and ImageNet-3DC [9] corruptions respectively. The exact listing of the
 104 network architectures can be found in the appendix D in Tab. 1.

105 3.1 PSF comparisons

106 Here, the complex optical kernels shall first be compared to the optical kernels visually in Fig 1 for
 107 all severities. Visually, the severities are comparable, even though there is a dependence on the color
 108 channel, as well as a break in rotational symmetry. A criterion to quantify the similarity are also the
 109 MTF50 values in Fig. 8. The values are similar and indicate an averaged comparability between the
 110 kernels. The MTF curves for the kernels can also be found in the appendix B. Note that for the optical
 111 kernels six different curves exist, which occur because of the direction dependence and wavelength
 112 dependence, whereas the complexity of the corruption kernels can be reduced to a single MTF curve.
 113 Astigmatic behavior can be read, for example, in severity 1 in appendix B, Fig. 6 in the red and blue
 114 channels, where either the 45° or the -45° curves proceed low. In addition, the orientations are just
 115 reversed, resulting in chromatic aberrations.

116 3.2 Image comparisons

117 The different filter kernels are then used to convolve the images from ImageNet and yield ten datasets
 118 of 50k images each. Both, images from corruption kernels and optical kernels are saved with the
 119 same slight JPEG compression as in ImageNet-C to avoid a corruption bias between lossless and
 120 lossy image data compression and to keep the processing of 500k images manageable. The usual
 121 transformations center crop and downscale to RGB images of size 224×224 are done as preprocessing
 122 step to the bigger original ImageNet images to ensure that no additional smoothing by the scaling
 123 operation is applied to the filtered images. The image samples in Fig. 1 visualize differences in the
 124 datasets corruption datasets and optical datasets. The blur in the images increases significantly with
 125 severities. Looking at optical datasets 2-4 color fringes at edges are readily visible and directional
 126 dependent blur occurs.

127 However, the mean values mMSE and mSSIM listed in 2 are very close to each other, which indicate
 128 similar and comparable image quality.

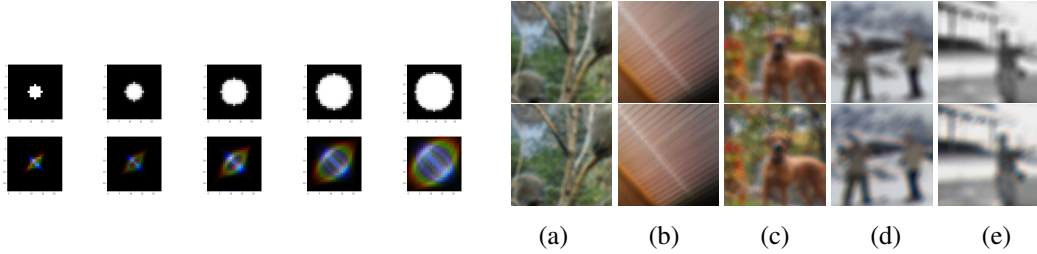


Figure 1: Left: PSFs representing the different "severities" 1-5 from left to right: First row visualizes the corruption kernels, the second row astigmatic optical kernels showing chromatic aberration. Right: Visual examples from the modified datasets with increasing severities: 2 (a), 3 (b-c) and 4 (d-e). The first row visualizes the effects of corruption kernels and the second of optical kernels. Read example: Chromatic aberration visible at the reddish and greenish branches (a) and at the window blind (b), while the simple kernels do not create color fringes.

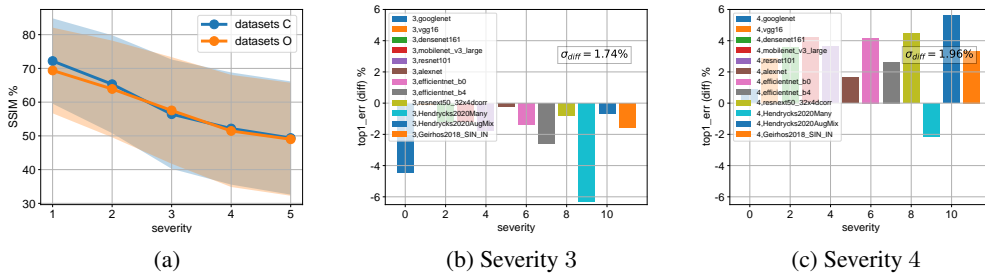


Figure 2: (a) Difference in mSSIM for all severities. The mSSIM for severities 3-5 is $\leq 1.1\%$. (b,c) Difference in top1-error between modified and unmodified ImageNet for corruption datasets and optical datasets. The average difference in mSSIM is below 1.1% for severities 3-5. Classification results (b,c) with a + denote worse classification for optical datasets (higher top1-error).

129 3.2.1 Classification on ImageNet

130 The images from corruption datasets and optical datasets are then processed with the different
 131 neural networks for classification from Tab. 1. Again, the processing is set such that no additional
 132 transformation besides image normalization is done, because the input size is already the target size
 133 of 224×224 . The classification results for 50k images each in Figs. 2b and 2c show differences of
 134 top1-errors for the selected neural networks. Looking at the mean values of the errors μ_{top1} , this bias
 135 can possibly be due to the slight variation between the kernel types: The image results show slight
 136 variations for levels 3 and 4 in mSSIM, respectively. For level 3, the mSSIM for optical datasets3 is
 137 higher (1.11 %) and for level 4, the mSSIM for corruption datasets4 is lower (-0.720%). However,
 138 significant differences between the networks can be found within these conditions. For example,
 139 Hendrycks2020Many[17, 18], as well as in most cases GoogLeNet[19], can handle the blur of optical
 140 kernels better than that of corruption kernels (lower top1-error). Hendrycks2020AugMix[20, 18] does
 141 mostly the opposite. All severities are visualized in appendix F. Note that the differences in mSSIM,
 142 mMSE, MTF50 and AUC are for severities 1-2 greater, but the top1-error deviation is smaller for
 143 these less blurred images.

144 4 Conclusion

145 This article compares the ImageNet validation dataset in several modified versions degraded with
 146 corruption kernels from ImageNet-C and optical kernels, which are directional and wavelength
 147 dependent. Although the blur kernels are of comparable size and produce similar image datasets,
 148 some classification results differ significantly. We conclude that realistic optical corruptions should
 149 be considered in our standard benchmarks towards model robustness.

References

- 150
- 151 [1] Dario Amodei et al. *Concrete Problems in AI Safety*. July 25, 2016. arXiv: 1606.06565 [cs].
- 152 [2] Philip Koopman and Michael Wagner. “Challenges in Autonomous Vehicle Testing and
- 153 Validation”. In: *SAE International Journal of Transportation Safety* 4.1 (Apr. 5, 2016), pp. 15–
- 154 24.
- 155 [3] Philip Koopman, Aaron Kane, and Jen Black. “Credible Autonomy Safety Argumentation”.
- 156 In: *Proceedings of the Safety-Critical Systems Symposium 2019* (), p. 27.
- 157 [4] Ian J. Goodfellow, Jonathon Shlens, and Christian Szegedy. *Explaining and Harnessing*
- 158 *Adversarial Examples*. Mar. 20, 2015. arXiv: 1412.6572 [cs, stat].
- 159 [5] Nicholas Carlini and David Wagner. “Adversarial Examples Are Not Easily Detected: By-
- 160 passing Ten Detection Methods”. In: *Proceedings of the 10th ACM Workshop on Artificial*
- 161 *Intelligence and Security*. CCS ’17: 2017 ACM SIGSAC Conference on Computer and Com-
- 162 munications Security. Dallas Texas USA: ACM, Nov. 3, 2017, pp. 3–14.
- 163 [6] Nicolas Papernot et al. “The Limitations of Deep Learning in Adversarial Settings”. In:
- 164 *2016 IEEE European Symposium on Security and Privacy (EuroS&P)*. 2016 IEEE European
- 165 Symposium on Security and Privacy (EuroS&P). Mar. 2016, pp. 372–387.
- 166 [7] Francesco Croce et al. “RobustBench: a standardized adversarial robustness benchmark”. In:
- 167 *Thirty-fifth Conference on Neural Information Processing Systems Datasets and Benchmarks*
- 168 *Track*. 2021.
- 169 [8] Dan Hendrycks and Thomas Dietterich. “Benchmarking Neural Network Robustness to Com-
- 170 mon Corruptions and Perturbations”. In: *arXiv:1903.12261 [cs, stat]* (Mar. 28, 2019). arXiv:
- 171 1903.12261.
- 172 [9] Oguzhan Fatih Kar et al. “3D Common Corruptions and Data Augmentation”. In: (), p. 12.
- 173 [10] Max Born and Emil Wolf. *Principles of optics: electromagnetic theory of propagation, interfer-*
- 174 *ence and diffraction of light*. 7th expanded ed. Cambridge ; New York: Cambridge University
- 175 Press, 1999. 952 pp.
- 176 [11] Joseph W. Goodman. *Introduction to Fourier optics*. Fourth edition. New York: W.H. Freeman,
- 177 Macmillan Learning, 2017. 546 pp.
- 178 [12] Glenn D. Boreman. *Modulation Transfer Function in Optical and Electro-Optical Systems*.
- 179 SPIE, July 1, 2001.
- 180 [13] *ISO12233:2017, Photography — Electronic still picture imaging — Resolution and spatial*
- 181 *frequency responses*. Standard. Volume: 2017. Geneva, CH: International Organization for
- 182 Standardization, 2017.
- 183 [14] Z. Wang et al. “Image Quality Assessment: From Error Visibility to Structural Similarity”. In:
- 184 *IEEE Transactions on Image Processing* 13.4 (Apr. 2004), pp. 600–612.
- 185 [15] Patrick Müller and Alexander Braun. “Simulating optical properties to access novel metro-
- 186 logical parameter ranges and the impact of different model approximations”. In: *2022 IEEE*
- 187 *International Workshop on Metrology for Automotive (MetroAutomotive)*. 2022 IEEE Inter-
- 188 national Workshop on Metrology for Automotive (MetroAutomotive). July 2022, pp. 133–
- 189 138.
- 190 [16] Alfredo Canziani, Adam Paszke, and Eugenio Culurciello. *An Analysis of Deep Neural Network*
- 191 *Models for Practical Applications*. Apr. 14, 2017. arXiv: 1605.07678 [cs].
- 192 [17] Dan Hendrycks et al. “The Many Faces of Robustness: A Critical Analysis of Out-of-
- 193 Distribution Generalization”. In: *2021 IEEE/CVF International Conference on Computer*
- 194 *Vision (ICCV)*. 2021 IEEE/CVF International Conference on Computer Vision (ICCV). Mon-
- 195 treal, QC, Canada: IEEE, Oct. 2021, pp. 8320–8329.
- 196 [18] Francesco Croce et al. *RobustBench: a standardized adversarial robustness benchmark*. Oct. 31,
- 197 2021. arXiv: 2010.09670 [cs, stat].
- 198 [19] Christian Szegedy et al. *Going Deeper with Convolutions*. arXiv:1409.4842. type: article.
- 199 arXiv, Sept. 16, 2014. arXiv: 1409.4842 [cs].
- 200 [20] Dan Hendrycks et al. *AugMix: A Simple Data Processing Method to Improve Robustness and*
- 201 *Uncertainty*. Feb. 17, 2020. arXiv: 1912.02781 [cs, stat].

202 **A PSFs**

203 The different used kernels are visualized in Figs. 3, 4 and 5.

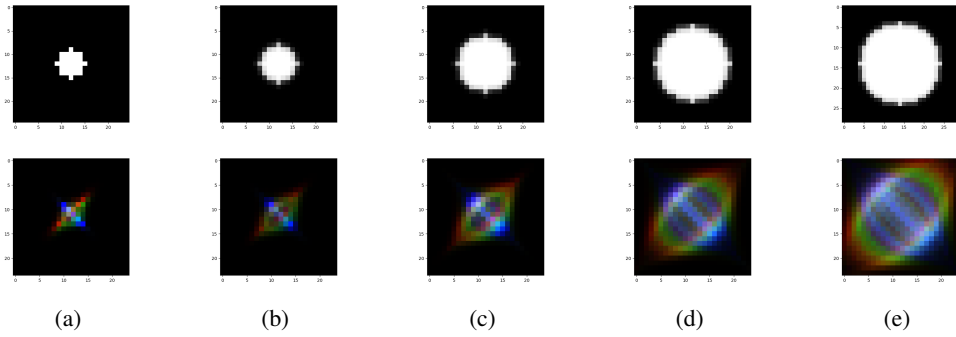


Figure 3: Average PSFs representing the different "severities" 1-5: (a-e) corruption kernels, (f-j) optical kernels with oblique astigmatism and chromatic aberrations.

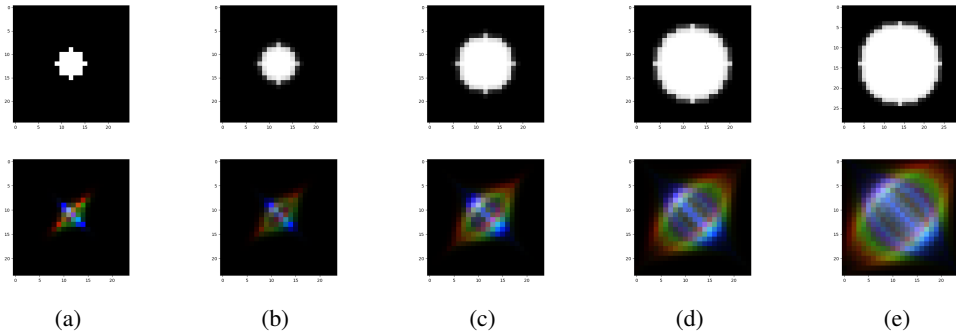


Figure 4: Average PSFs representing the different "severities" 1-5: (a-e) corruption kernels, (f-j) optical kernels with oblique astigmatism and chromatic aberrations. These kernels have higher match quality and minimize mSSIM on the datasets, although visually hard to distinct from Fig. 3

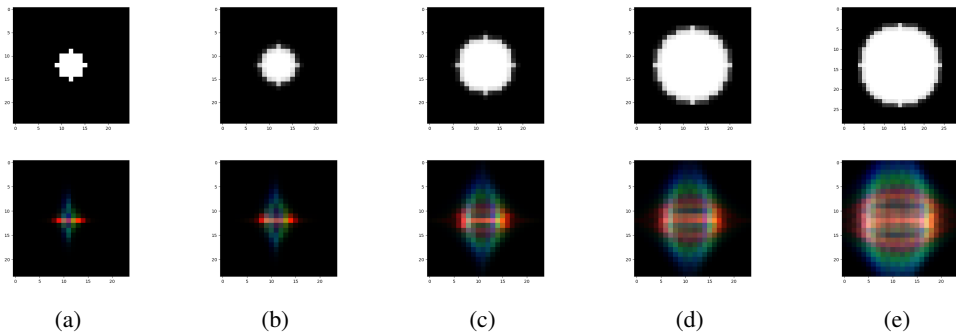


Figure 5: Average PSFs representing the different "severities" 1-5: (a-e) corruption kernels, (f-j) optical kernels with straight astigmatism and chromatic aberrations.

204 **B MTF curves**

205 Here, the direction in coordinate axes is denoted with (x, y) and the diagonal direction is denoted with
 206 $\pm 45^\circ$. Note that sometimes curves for the optical kernels in different directions proceed differently.
 207 This astigmatic behaviour is color channel dependent and therefore creates chromatic aberrations.

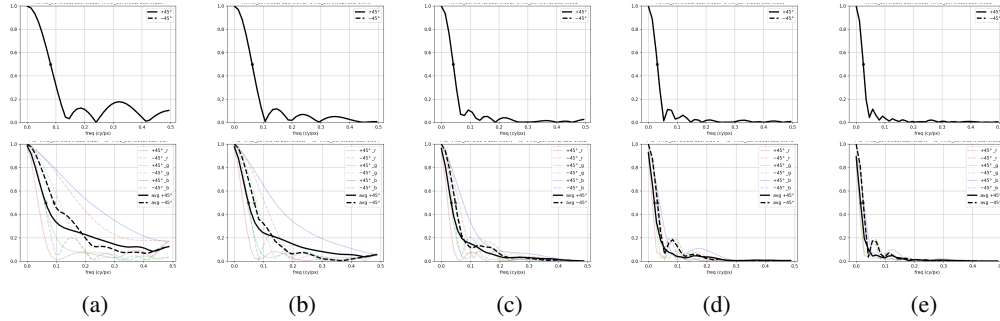


Figure 6: MTF slices from PSFs for severities (1-5, a-e): First row corruption kernels, second row optical kernels with oblique astigmatism from Fig. 3

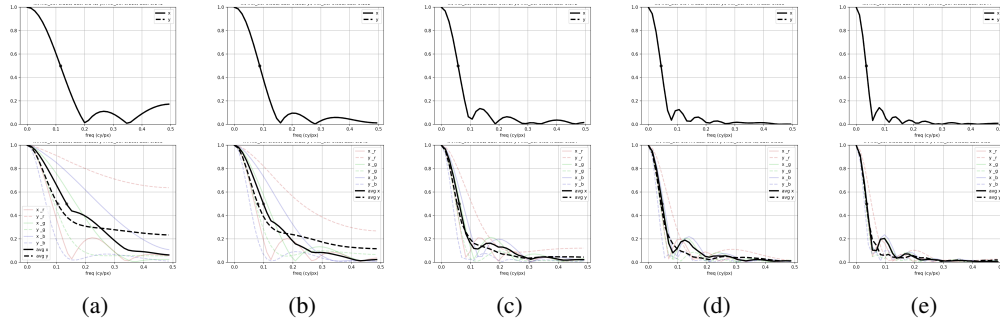


Figure 7: MTF slices from PSFs for severities (1-5, a-e): First row corruption kernels, second row optical kernels with straight astigmatism ($0^\circ, 90^\circ$) from Fig. 5

208 **B.1 Aggregated MTF metrics - differences for MTF50**

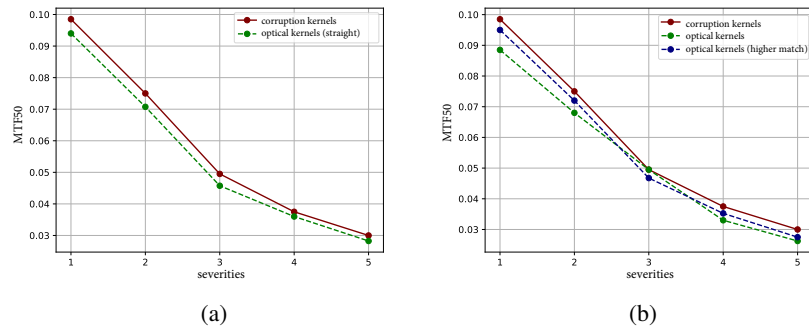


Figure 8: MTF50 values for all severities and the different studies: (a) visualizes corruption kernels vs. optical kernels with straight astigmatism from Fig. 5 and (b) displays the optical kernels from Fig. 3 and 4. Each point is acquired by averaging color, orientation and direction to get a single MTF from the above MTF curves from Figs. 7 and 6. From this resulting MTF the MTF50 value is taken. We also show the MTF50 values from curves with minimum mSSIM on the datasets.

209 **C Additional studies for different optical kernels**

210 **C.1 Oblique astigmatism (higher match quality)**

211 We provide here a version with closer match in mSSIM, mMSE, MTF50 and AUC for all severities
 212 with the parameterization $A_2^{-2} \in \{0.9, 1.3, 2.1, 2.8, 3.6\} \lambda_i$. The mSSIM for severities 3-5 is below
 213 0.5 %, but although significantly smaller differences occur compared to Fig. 14 still the DNNs can
 214 handle the blur types differently well, which indicates a distribution shift. Lower severities tend to be
 more robust to changes in mSSIM and the improved match quality has little effect.

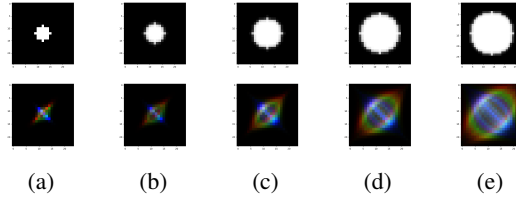


Figure 9: Average PSFs representing the different "severities" 1-5. First row: corruption kernels with higher match quality, second row: optical kernels with chromatic aberrations.

215

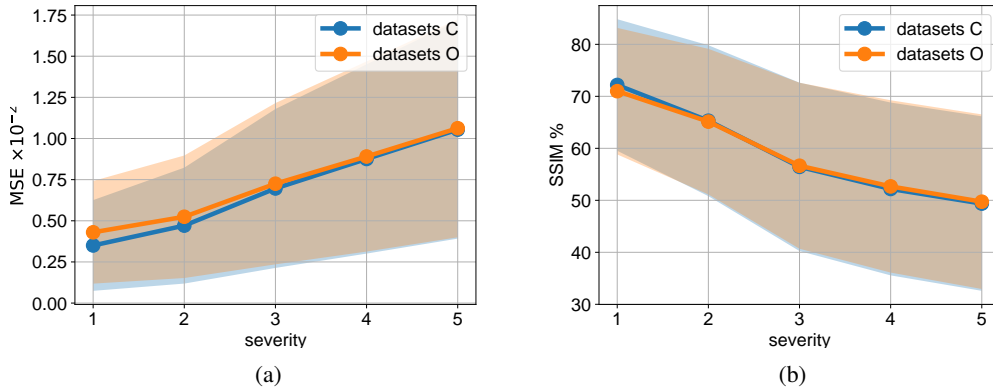


Figure 10: Average MSE (a) and SSIM (b) between corrupted image database and unmodified original.

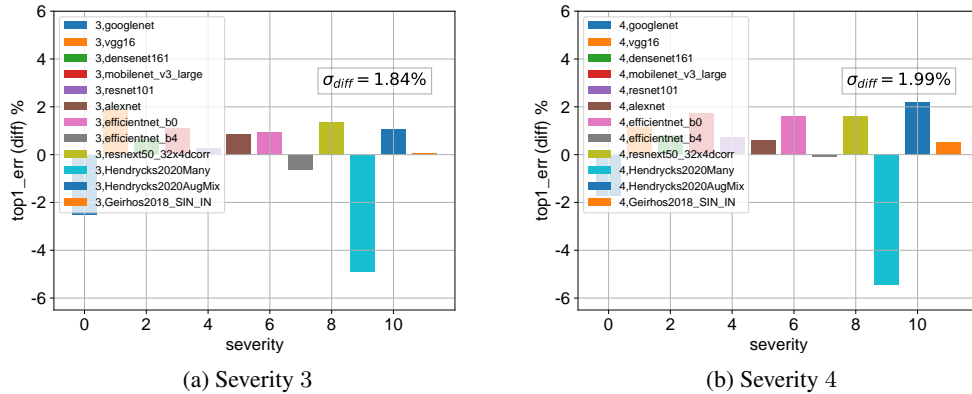


Figure 11: Deviation in top1-error for all neural networks and severities 3 and 4. "+" means that optical datasets have higher top1-error than corruption datasets.

216 **C.2 Oblique astigmatism**

217 We include here the study on oblique astigmatic optical kernels as used in the main article. The size
 218 of the kernels in Fig. 3 look very similar to Fig. 4, but create a slightly larger mSSIM $\leq 1.1\%$ for
 severities 3-5.

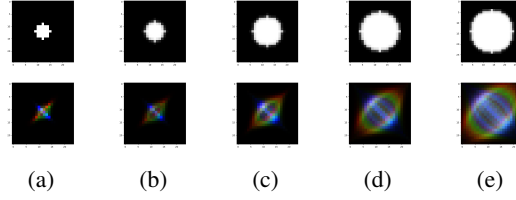


Figure 12: Average PSFs representing the different "severities" 1-5. First row: corruption kernels, second row: optical kernels with chromatic aberrations.

219

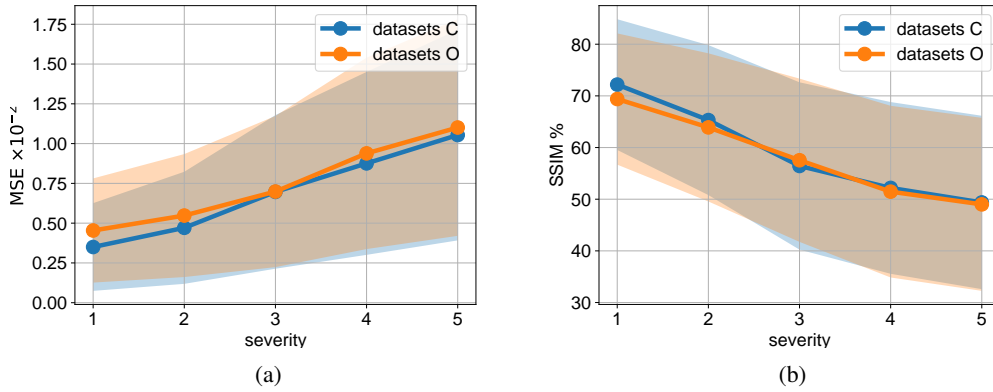


Figure 13: Average MSE (a) and SSIM (b) between corrupted image database and unmodified original.

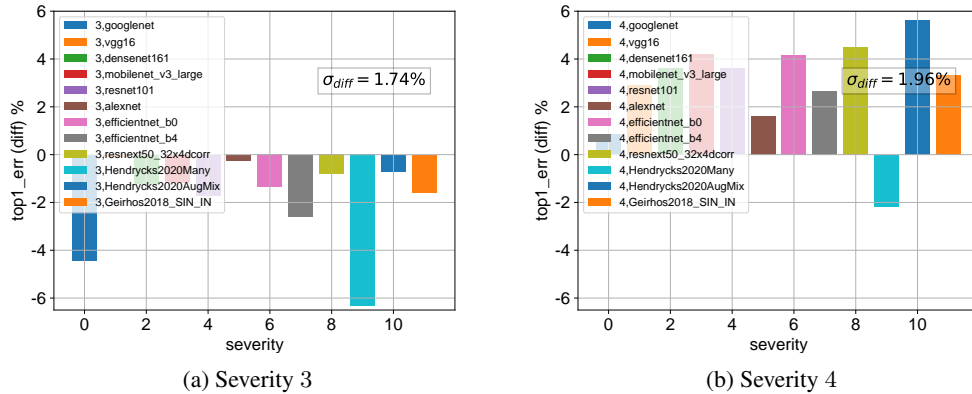


Figure 14: Deviation in top1-error for all neural networks and severities 3 and 4. "+" means that optical datasets have higher top1-error than corruption datasets.

220 **C.3 Straight astigmatism**

221 This study shows the effect of the parameterization of straight astigmatism $A_2^{+2} \in$
 222 $\{1.0, 1.4, 2.2, 2.8, 3.6\}\lambda_i$, which leads to comparable results as in Fig. 11.

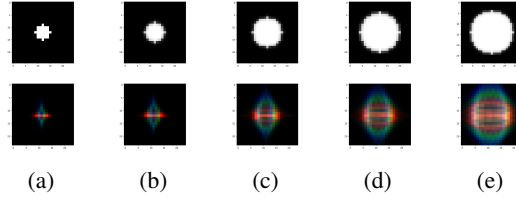


Figure 15: Average PSFs representing the different "severities" 1-5. First row: corruption kernels, second row: optical kernels with chromatic aberrations.

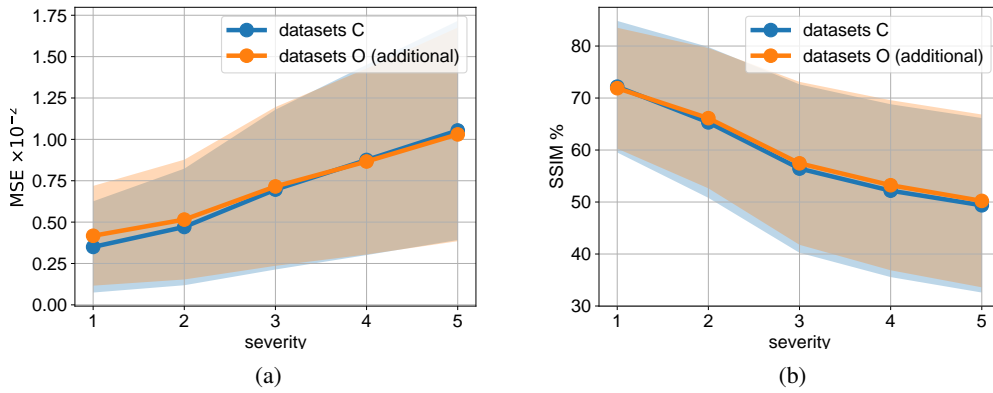


Figure 16: Average MSE (a) and SSIM (b) between corrupted image database and unmodified original.

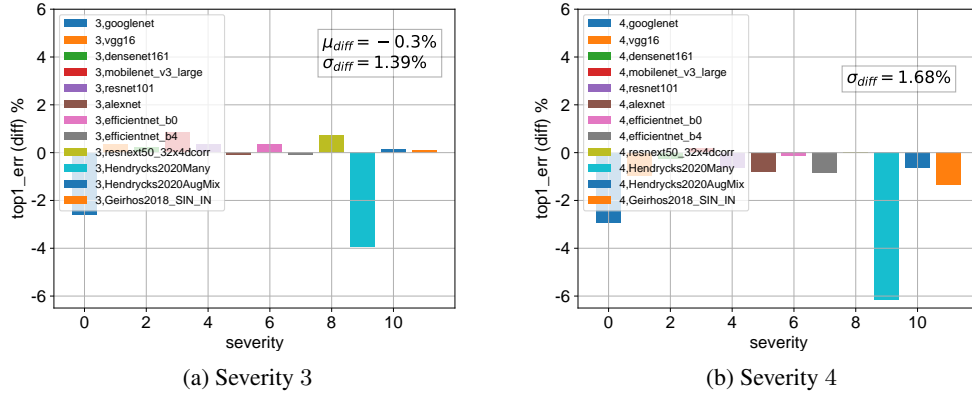


Figure 17: Deviation in top1-error for all neural networks and severities 3 and 4. "+" means that optical datasets have higher top1-error than corruption datasets. Difference in mSSIM $\leq 1\%$.

223 **D Additional tables**

Table 1: Selection of pretrained models from pytorch vision and RobustBench model zoos with corresponding number of trainable parameters. The selected neural networks from RobustBench use a Resnet50.

Name	Number of Parameters [$\times 10^6$]	Name	Number of Parameters [$\times 10^6$]
VGG16	138.4	ResNeXt50	25.0
AlexNet	61.1	EfficientNet_B4	19.3
ResNet101	44.5	GoogLeNet	6.6
DenseNet161	28.7	MobileNet_v3	5.5
Resnet50	25.6	EfficientNet_B0	5.3

224 **E Additional image examples**

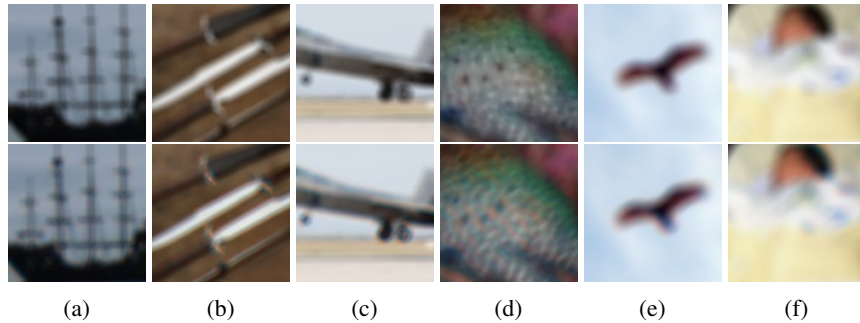


Figure 18: All images are zoomed in. First row corruption datasets, second row optical datasets. Severity 3 (a-c): Chromatic aberration visible at the airplanes wheels, the dog’s face, the window blind and the boat’s mast. Note also the diagonal astigmatism. Severity 5: (d-e) visible chromatic aberration at the fish scales as orange stripes, the eagle, and as color fringe at the baby’s hair.

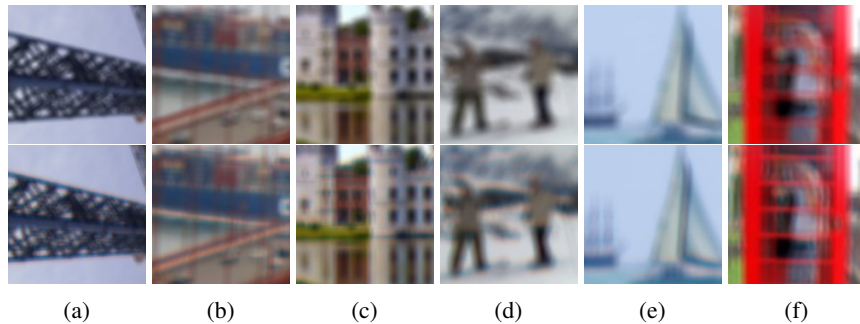


Figure 19: First row corruption datasets, second row optical datasets (straight). Severity 3 (a-c): Chromatic aberration visible at the airplanes wheels, the dog’s face, the window blind and the boat’s mast. Note also the diagonal astigmatism. Severity 5: (d-e) visible chromatic aberration at the fish scales as orange stripes, the eagle, and as color fringe at the baby’s hair.

225 **F Classification results for all severities**

Below the classification results are plotted for the two studies.

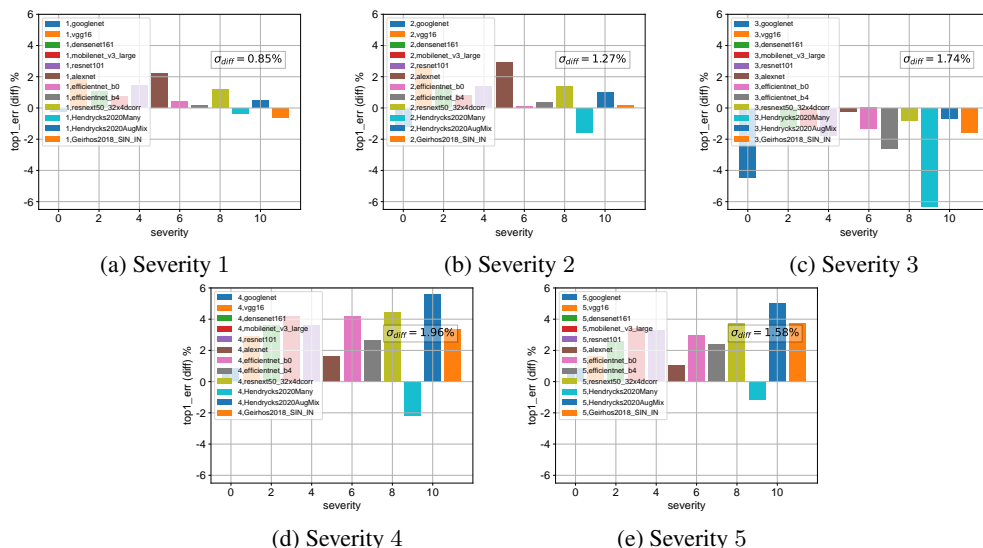


Figure 20: Classification results, difference in top1-error in percentage points: Comparison of optical datasets and corruption datasets for severities 1-5 from (a-e). Difference in mSSIM $\leq 1.1\%$ for severities 3-5.

226

227 **F.1 Classification results for all severities for additional studies**

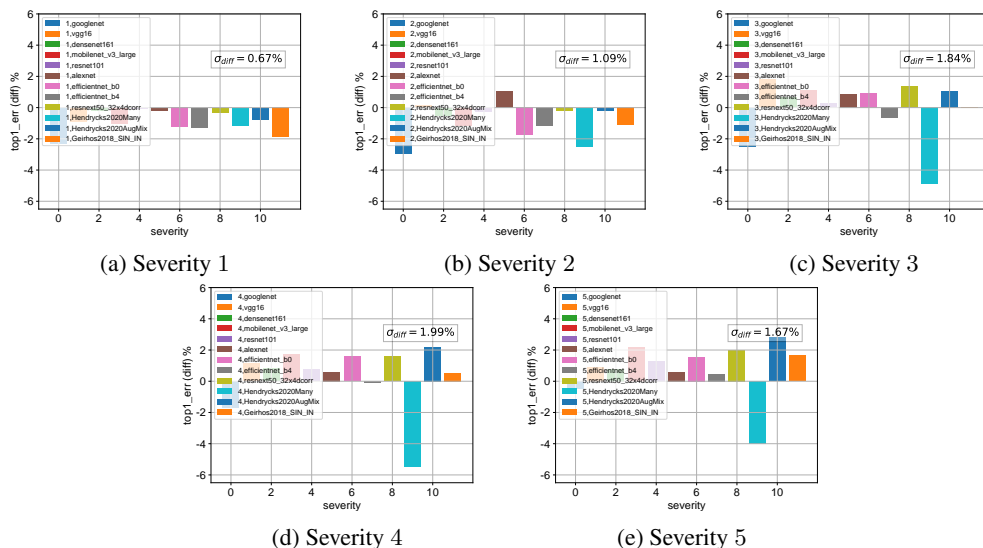


Figure 21: Classification results, difference in top1-error in percentage points: Comparison of optical datasets and corruption datasets using optical kernels *with higher match quality* for severities 1-5 from (a-e). Difference in mSSIM $\leq 0.5\%$ for severities 3-5.

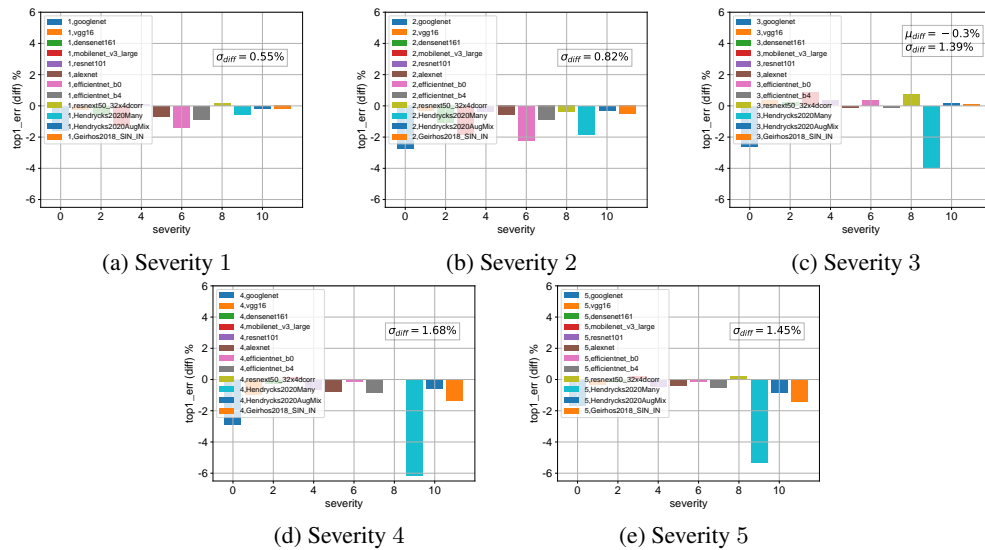


Figure 22: Classification results, difference in top1-error in percentage points: Comparison of optical datasets with straight astigmatism and corruption datasets for severities 1-5 from (a-e). Difference in mSSIM $\leq 1\%$.

228 **F.2 Absolute results on the different modified dataset versions**

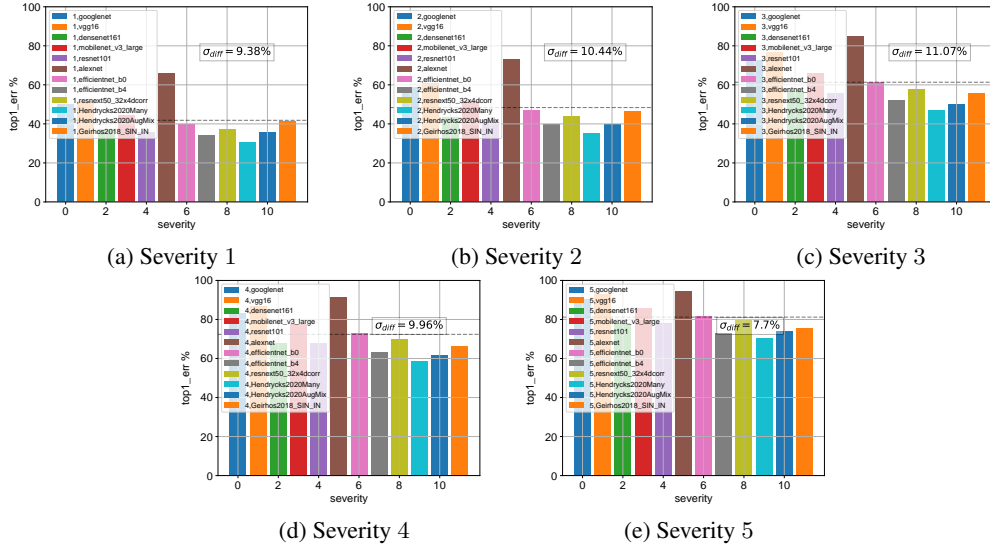


Figure 23: Classification results: Top1-error for corruption kernels for severities 1-5 from (a-e).

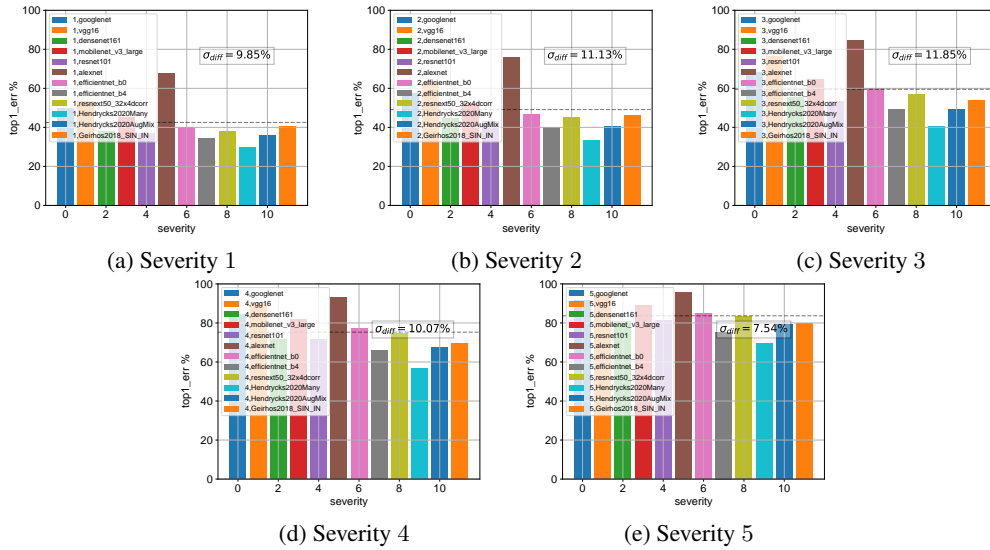


Figure 24: Classification results: Top1-error for optical kernels (oblique astigmatism) from Fig. 3 for severities 1-5 from (a-e). Difference in mSSIM \leq for 1.1 % for severities 3-5.

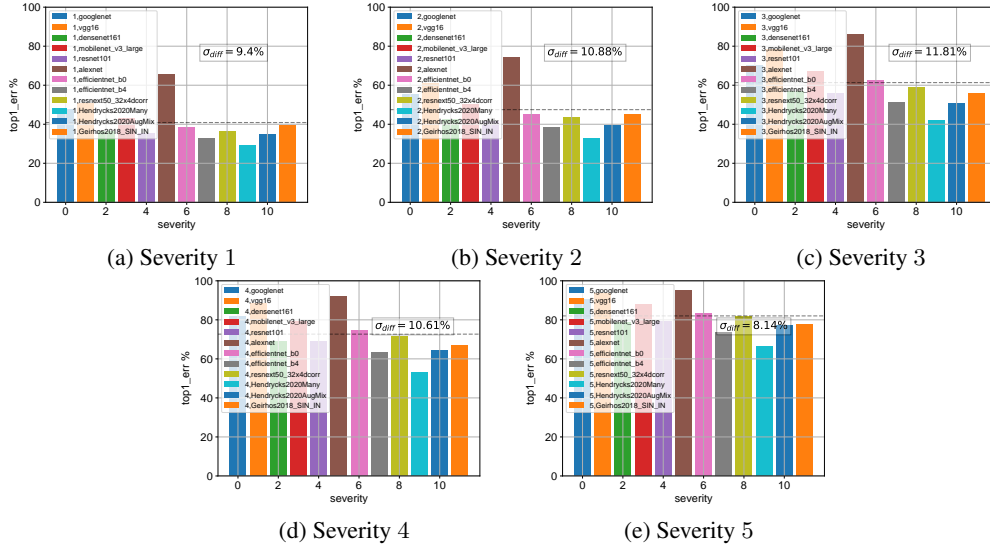


Figure 25: Classification results: Top1-error in percentage points: optical datasets with optical kernels from Fig. 4 with higher match quality for severities 1-5 from (a-e). Difference in mSSIM $\leq 0.5\%$ for severities 3-5.

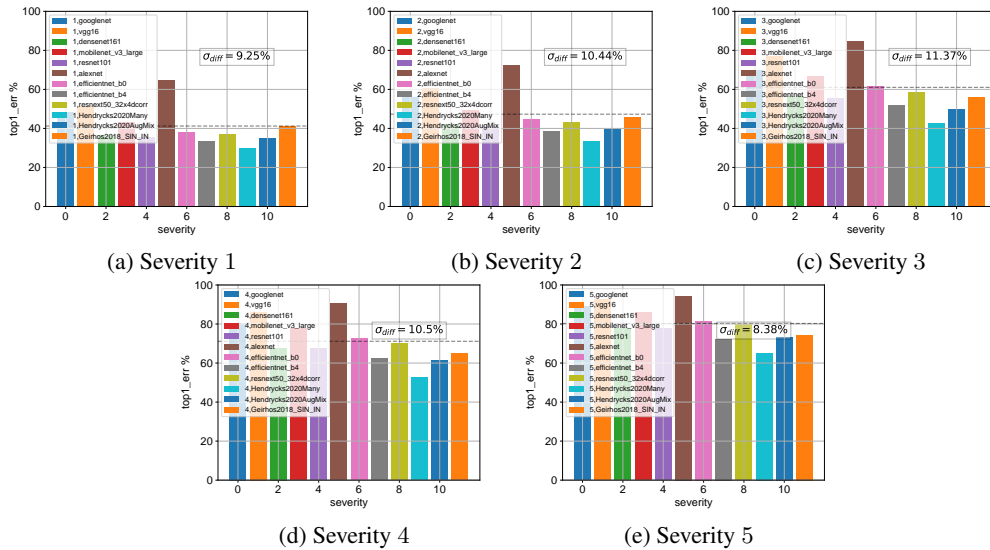


Figure 26: Classification results: Top1-error in percentage points for optical datasets with straight astigmatism from Fig. 5 for severities 1-5 from (a-e). Difference in mSSIM $\leq 1\%$.